Eurographics Conference on Visualization (EuroVis) 2017
J. Heer, T. Ropinski and J. van Wijk
(Guest Editors)

Volume 36 (2017), Number 3

Overview + Detail Visualization for Ensembles of Diffusion Tensors

C. Zhang[1], M.W.A. Caan[2], T. Höllt[1,3], E. Eisemann[1], A. Vilanova[1]

[1]Computer Graphics and Visualization, Delft University of Technology, Delft, The Netherlands
[2]Brain Imaging Center, Academic Medical Center, University of Amsterdam, Amsterdam, The Netherlands
[3]Computational Biology Center, Leiden University Medical Center, Leiden, The Netherlands

Abstract

A diffusion tensor imaging group study consists of a collection of volumetric diffusion tensor datasets (i.e., an ensemble) acquired from a group of subjects. The multivariate nature of the diffusion tensor imposes challenges on the analysis and the visualization. These challenges are commonly tackled by reducing the diffusion tensors to scalar-valued quantities that can be analyzed with common statistical tools. However, reducing tensors to scalars poses the risk of losing intrinsic information about the tensor. Visualization of tensor ensemble data without loss of information is still a largely unsolved problem. In this work, we propose an overview + detail visualization to facilitate the tensor ensemble exploration. We define an ensemble representative tensor and variations in terms of the three intrinsic tensor properties (i.e., scale, shape, and orientation) separately. The ensemble summary information is visually encoded into the newly designed aggregate tensor glyph which, in a spatial layout, functions as the overview. The aggregate tensor glyph guides the analyst to interesting areas that would need further detailed inspection. The detail views reveal the original information that is lost during aggregation. It helps the analyst to further understand the sources of variation and formulate hypotheses. To illustrate the applicability of our prototype, we compare with most relevant previous work through a user study and we present a case study on the analysis of a brain diffusion tensor dataset ensemble from healthy volunteers.

Categories and Subject Descriptors (according to ACM CCS): I.3.5 [Computer Graphics]: —Curve, surface, solid, and object representations I.3.8 [Computer Graphics]: Applications—

1. Introduction

Diffusion Tensor Imaging [BML94] (DTI) is an imaging modality that models water diffusion as a second-order positive-definite tensor. It enables the characterization of anatomical fibrous structures. DTI is extensively used by neuroscientists to study the structural connectivity of the brain. Nowadays, studies are often carried out using multiple, registered DTI datasets, also called cohorts or ensembles [SPB07, WWHT07, DJB*11, MBW*11], for example, in order to locate variations in the datasets between subjects that might be caused by anatomical variation or pathology.

However, due to the complexity of multivariate statistical analysis of tensors, most of the existing approaches are based on derived scalar quantities, such as fractional anisotropy [BP96] (FA), rather than the multivariate diffusion tensor itself. The analysis of derived scalar quantities provides merely one facet of the full information that a diffusion tensor contains. Simultaneous visual inspection of several scalar quantities is possible, for example, with side-by-side views, but meaningful relationships are hard to identify in such a setting. The few available approaches that focus on the diffusion tensor as a whole [BP03, BP07, AWHS16] assume a normal distribution of tensors within the ensemble. However, the normal distribution assumption is not always valid, and the statistical summary (i.e., fourth-order covariance tensor) is difficult to interpret.

In this paper, we make the concept of the intrinsic properties (i.e., scale, shape, and orientation) of diffusion tensors available for the analysis and visualization of DTI ensembles to facilitate their interpretation. A major challenge for this approach is to deal appropriately with the inherently coupled relation between shape and orientation. The main contribution of this work is an integrated overview + detail visual analysis framework for the exploration of DTI ensembles that does not assume any specific distribution of the underlying data.

- We propose a representative tensor that is derived by separately aggregating the intrinsic properties, instead of using the Euclidean mean that treats these properties collectively.
- Variation within the tensor ensemble is defined based on the pair-wise difference measures of the three tensor intrinsic properties [ZSL*16].
- We extend two existing glyph-based visualizations [Kin04, PPvA*09] to encode variation uncovered in the ensemble.
- We present a detail visualization that enables intuitive exploration of the tensor ensemble, separately for the tensor intrinsic properties, without assuming a specific distribution.

2. Related Work

Glyph-based Visualization for Diffusion MRI. A diffusion tensor (i.e., a 3×3 symmetric positive-definite matrix) is a multivariate physical quantity. Glyph-based visualization is a natural choice for displaying the full tensor information at discrete locations due to its ability to effectively encode multivariate attributes. Multiple glyph designs (e.g., ellipsoids [PB96], composite shapes [WMK*99], superquadrics [Kin04]) are introduced for the visualization of a single tensor. Overlaying glyphs is a commonly used strategy to compare two tensors [AWHS16, MVB*17]. For the same purpose, Zhang et al. [ZSL*16] propose a checkerboard-style superquadrics-based glyph to facilitate the comparison. For an ensemble of tensors, Jones et al. [JGA*02] simply overlay multiple glyphs while Abbasloo et al. [AWHS16] employ animation of glyphs.

Another diffusion MRI modeling technique is high angular resolution diffusion imaging (HARDI). Unlike DTI, it enables the reconstruction of multiple major diffusion directions. HARDI data represents the diffusion orientation distribution function (dODF), i.e., the probability that a water molecule moves in a given direction after a given amount of time. Several glyph designs are introduced for this data. Peeters et al. [PPvA*09] render HARDI data as a deformed sphere by GPU-based ray-casting. Schultz and Kindlmann [SK10a] present the higher-order maximum enhancing (HOME) glyph for HARDI data by generalizing tensor ellipsoid.

In our work, we extend the glyph designs of Kindlmann [Kin04] and Peeters et al. [PPvA*09] to additionally encode the variation information of diffusion tensor ensembles.

Ensemble/Uncertainty Visualization. Ensembles are commonly used for assessing uncertainty and variability, for instance, in weather forecasting [SZD*10]. Ensemble visualization and uncertainty visualization are often discussed together [LPK05, BHJ*14]. For scalar fields, uncertainty information is often presented as the variation of isocontours, such as the spaghetti plot [PWB*09] or contour boxplot [WMK13], or as isosurfaces as presented by Pöthkow et al. [PH11, PWH11] and Pfaffelmoser et al. [PRW11]. Djurcilov et al. [DKLP01] directly visualize scalar field uncertainty in direct volume rendering. For vector fields, curve boxplots [MWK14] and streamline variability plots [FBW16] focus on the variation of features extracted from the field, rather than the field itself. Botchen et. al. [BWE05] use a 3D noise texture of different frequencies to visualize vector uncertainty in flow fields. Otto et al. [OGT11] analyze the global uncertainty in the 3D vector fields by a topological approach. For the visual analysis of an ensemble of ODFs, Jiao et al. [JPGJ12] use direct volume rendering based on the so-called shape inclusion probability function.

Glyphs are commonly used to visualize multivariate local attributes of ensemble data. Potter et al. [PKRJ10] present a new hybrid summary plot that incorporates descriptive statistics. Höllt et al. [HMZ*14] use a glyph, based on the violin plot, to indicate variation in multiple ensemble variables for time series visualization. Pfaffelmoser et al. [PMW13] present uncertainty in gradient orientation within scalar-field ensembles using circular glyphs. Hlawatsch et al. [HLNW11] introduce the flow radar glyph to display possible ranges of flow directions. Jarema et al. [JDKW15] use glyphs to show modality information of circular distributions in 2D vector fields ensemble.

The methods presented in this subsection can be used for visualizing the variation of tensor-derived features (e.g., principle diffusion direction or FA). However, we focus on the visualization of the full diffusion tensor information without information reduction.

Visual Analysis of Diffusion Tensor Ensembles. There is a limited amount of work that focuses on the visual analysis of ensembles of diffusion tensors in its entirety. In order to aggregate the ensemble information, multivariate statistics can be used. Basser and Pajevic [BP03, BP07] propose the use of the fourth-order covariance tensor based on the assumption that the set of diffusion tensors follows a multivariate normal distribution. The fourth-order covariance tensor represents deviations from the mean tensor, which is built by component-wise averaging. High-order tensors can be projected onto a unit sphere via tensor contraction and thus visualized as a deformed sphere, referred to as radial glyph [BP07]. Basser and Pajevic [BP07] use radial glyphs to visualize the fourth-order tensor and its six orthogonal second-order eigentensors or eigenmodes. The six mutual orthogonal eigentensors represent all modes of tensor variation. However, this visual encoding is difficult to interpret. In recent work, Abbasloo et al. [AWHS16] combine slice views, volume rendering, and superquadric glyphs [Kin04] to visualize the fourth-order covariance tensor at multiple levels of detail. In order to facilitate the interpretation of the covariance tensor, they use the decomposition framework proposed by Kindlmann et al. [KEWW07]. The framework is based on the gradients of meaningful tensor invariants. They visualize the six orthogonal eigentensors, which contain a mixture of different tensor intrinsic properties, through animation. Eigentensors allow the identification of correlations but also provide potentially misleading interpretations in some situations (e.g., in the cases shown in Section 8.1).

Our work enriches this area by aggregating tensor ensembles to a representative mean tensor and variations based on the three tensor intrinsic properties without resorting to the fourth-order covariance tensor. Our extended tensor glyph design enables a clear interpretation of the mean tensor and its variations, even though it does not allow for detection of potential correlations between the tensor intrinsic properties. We also design visual analysis strategies to explore the ensemble elements in detail in terms of the intrinsic properties and discover their potential correlations.

3. Summary Statistics for Diffusion Tensor Ensembles

In order to aggregate or summarize an ensemble of diffusion tensors, we resort to statistical tools. In this section, we introduce and motivate our statistical analysis approaches.

We define the space of symmetric tensors in $\mathbb{R}^3$ as Sym_3 and the corresponding tensor field as $\mathbf{F}: \mathbb{R}^3 \to \mathrm{Sym}_3$. An ensemble of n diffusion tensor fields is denoted by $\{\mathbf{F}_i\}_{i=1}^n$. Since our focus is voxel-wise analysis, the main object of interest is a set of tensors at a specific location $\mathbf{x}$ within the field, denoted by $\{\mathbf{F}_i(\mathbf{x})\}_{i=1}^n$. For simplicity, we denote the set as $\{\mathbf{D}_i\}_{i=1}^n$, and refer to it as a *tensor ensemble*. Notice that most of the solutions presented in this paper are also valid for ensembles of any second-order positive-definite tensors independent of their origins.

3.1. Diffusion Tensor Decomposition

The exact way of decomposing a tensor is dependent on the application. For diffusion tensors, an informative and intuitive decomposition consists of three intrinsic properties (i.e., scale, shape, and orientation). Each of these properties carries a specific interpretation about the underlying fiber structures. Decomposition into these three intrinsic properties is well studied [EK06, ZSL*16]. Hence, we briefly introduce the decomposition as proposed by Zhang et al. [ZSL*16] here.

A symmetric and positive-definite diffusion tensor $\mathbf{D}$ can be eigen-decomposed into three sorted real eigenvalues $\lambda_1 \geq \lambda_2 \geq \lambda_3 \geq 0$ where λ_1 is often referred to as the *main* or *major* eigenvalue. The orthonormal eigenvectors are ordered accordingly $(\mathbf{e}_1, \mathbf{e}_2, \mathbf{e}_3)$. The tensor trace, $\mathrm{tr}(\mathbf{D})$, is defined as the sum of the eigenvalues $\mathrm{tr}(\mathbf{D}) = \sum_{j=1}^{3} \lambda_j$, and is proportional to a commonly used tensor invariant called mean diffusivity [BP96]. Finally, the sorted normalized eigenvalues $\left(\tilde{\lambda}_1, \tilde{\lambda}_2, \tilde{\lambda}_3\right)$ are given by $(\lambda_1, \lambda_2, \lambda_3) / \mathrm{tr}(\mathbf{D})$.

A diffusion tensor has six degrees-of-freedom (DOFs) in total. Tensor scale, one DOF, can be represented by the trace $\mathrm{tr}(\mathbf{D})$ and has a range of $[0, \infty)$. It indicates the overall amount of diffusion. There is more diffusion in regions without fibers (e.g., ventricle) than with fibers (e.g., corpus callosum). Tensor shape, two DOFs, can be represented by the sorted normalized eigenvalues $\left(\tilde{\lambda}_1, \tilde{\lambda}_2, \tilde{\lambda}_3\right)$ with range $[0, 1]$, reflecting the underlying fiber configurations (e.g., a single fiber population or two crossing fiber populations). Tensor orientation is given by the set of eigenvectors $(\mathbf{e}_1, \mathbf{e}_2, \mathbf{e}_3)$. The major eigenvector $\mathbf{e}_1$ is empirically assumed to be aligned with the underlying fiber pathways. Shape and orientation are inherently coupled. For example, if the tensor shape is isotropic (i.e., three equal eigenvalues), the orientation is completely undefined. This fact complicates the decomposition and the subsequent statistical analysis.

3.2. Diffusion Tensor Ensemble Aggregation

We characterize a tensor ensemble by *separately* deriving the mean and standard deviation for scale, shape, and orientation. Given its special characteristics, we also propose an alternative that does not rely on the mean and standard deviation of the orientation. Instead, we estimate the diffusion orientation distribution function (dODF) according to the normal distributions implied by each tensor of the ensemble. This approach enables the depiction of multiple orientations within the ensemble.

3.2.1. Tensor Ensemble Mean

We first consider the special case of calculating the mean on an ensemble consisting of just two tensors. Here, the mean tensor can simply be viewed as an interpolation between two tensors. Kindlmann et al. [KSJEN*07] illustrate that Euclidean as well as Log-Euclidean interpolation cannot guarantee a monotonic interpolation of the tensor shape invariants, and as such can introduce spurious tensor shapes. Extending the Euclidean mean to more than two ensemble members corresponds to computing a component-wise average. Although it has been used in previous work [BP03, AWHS16], the Euclidean mean has undesired properties [KSJEN*07]. Let us consider an ensemble of linear anisotropic tensors with exactly the same eigenvalues but different eigenvectors, as shown in Figure 1a. It can be observed that the Euclidean mean tensor (Figure 1b) has a spurious shape that is not present in the original ensemble. Such a shape can mislead the analyst to make false assumptions about the underlying ensemble. Therefore, we propose to derive the mean tensor by computing the average of the three intrinsic properties *separately* and then combine them to form the mean tensor. Therefore, the characteristics are preserved and can be analyzed in the mean tensor. We denote this new mean tensor as $\overline{\mathbf{D}}$.

The trace of $\overline{\mathbf{D}}$ is defined as the average of individual tensor traces,

$$\mathrm{tr}\left(\overline{\mathbf{D}}\right) = \frac{1}{n} \sum_{i=1}^{n} \mathrm{tr}\left(\mathbf{D}_i\right). \tag{1}$$

Note that $\mathrm{tr}\left(\overline{\mathbf{D}}\right)$ is identical to the trace of the Euclidean mean.

Because of the normalization and sorting, all possible eigenvalue tuples $\left(\tilde{\lambda}_1, \tilde{\lambda}_2, \tilde{\lambda}_3\right)$, representing the shape, form a plane in $\mathbb{R}^3$ (see Figure 2). Therefore, the shape of $\overline{\mathbf{D}}$ is defined as

$$\left(\tilde{\lambda}_1, \tilde{\lambda}_2, \tilde{\lambda}_3\right)^{\overline{\mathbf{D}}} = \frac{1}{n} \sum_{i=1}^{n} \left(\tilde{\lambda}_1, \tilde{\lambda}_2, \tilde{\lambda}_3\right)^{\mathbf{D}_i}. \tag{2}$$

The superscript indicates the corresponding tensor from which the normalized eigenvalues are derived. Our idea is similar to Gahm et al. [GWK*12], but we aim at summarizing the tensor ensemble members while they focus on pair-wise tensor interpolation. Furthermore, we work directly with the eigenvalues instead of specific tensor invariants.

So far we have defined scale and shape of the mean tensor, which represent the mean diffusion amount and mean diffusion shape, respectively. However, the definition of the mean orientation is not as straightforward as the mean scale and shape because the eigenvectors are not always well-defined (i.e., in the case of two or three equal eigenvalues), and do not have a unique sign. In order to construct the complete mean tensor, a set of eigenvectors $(\mathbf{e}_1, \mathbf{e}_2, \mathbf{e}_3)^{\overline{\mathbf{D}}}$ is required to orient the mean tensor in the 3D domain. Here, we use the eigenvectors of the Euclidean mean $(\mathbf{e}_1, \mathbf{e}_2, \mathbf{e}_3)^{\mathrm{Eu}}$ as the eigenvectors of our mean tensor, as suggested by Gahm et al. [GWK*12]. The orientation of the mean tensor can provide

Figure 1: *Two types of mean tensors for (a) 10 linear anisotropic tensors with the same eigenvalues* $(0.7, 0.15, 0.15)$ *but different eigenvectors. (b) is the Euclidean mean and (c) is the ensemble mean calculated according to Equation* (3).

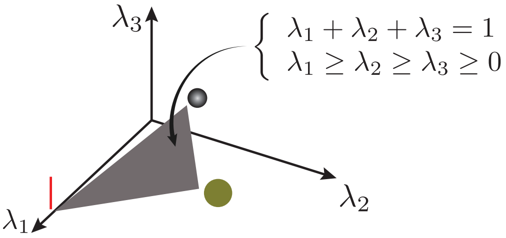

Figure 2: *Tensor shape space is defined by the sorted and normalized eigenvalues* $\tilde{\lambda}_j$*. Three glyphs are placed at the corners as reference, colored according to their* $\tilde{\lambda}_j$*.*

anatomical reference that is relevant for the understanding of the context. However, strongly diverging orientations in the ensemble can get lost. Therefore, the orientation has to be analyzed with care.

Finally, the separate components are assembled into the mean tensor as,

$$\overline{\mathbf{D}} := \mathrm{tr}\left(\overline{\mathbf{D}}\right) \sum_{j=1}^{3} \tilde{\lambda}_j^{\overline{\mathbf{D}}}\, \mathbf{e}_j^{\overline{\mathbf{D}}} \otimes \mathbf{e}_j^{\overline{\mathbf{D}}}. \tag{3}$$

By separately handling scale, shape, and orientation, we effectively avoid the introduction of tensor intrinsic properties that are not present in the tensor ensemble into the mean tensor. Figure 1c shows the mean tensor of the ensemble introduced in Figure 1a, calculated according to Equation (3). This new mean tensor preserves the shape of the tensors in the ensemble.

However, $(\mathbf{e}_1, \mathbf{e}_2, \mathbf{e}_3)^{\mathrm{Eu}}$ can be ill-defined and do not give a good representation of the underlying ensemble orientation. For example, consider a second ensemble of linear tensors, consisting of orthogonal pairs in Figure 3a. The Euclidean mean in Figure 3b of this ensemble has a planar shape. Thus its eigenvectors $(\mathbf{e}_1, \mathbf{e}_2, \mathbf{e}_3)^{\mathrm{Eu}}$ cannot be uniquely defined. The mean tensor, according to Equation (3), will have a clear linear shape, but an *arbitrary* and *meaningless* orientation.

Alternatively, we propose to summarize the orientation based on the diffusion orientation distribution function (dODF) that can be analytically expressed [ALS*10] as

$$\begin{aligned} p(\mathbf{r}) &= \frac{1}{(2\pi)^{\frac{3}{2}} |\mathbf{D}|^{\frac{1}{2}}} e^{-\frac{1}{2}\mathbf{r}^{\mathrm{T}}\mathbf{D}^{-1}\mathbf{r}}, \\ \mathrm{dODF}(\mathbf{u}) &= \int_0^{\infty} P(r\mathbf{u})\, r^2 dr = \frac{1}{4\pi|\mathbf{D}|^{\frac{1}{2}} \left(\mathbf{u}^{\mathrm{T}}\mathbf{D}^{-1}\mathbf{u}\right)^{\frac{3}{2}}}. \end{aligned} \tag{4}$$

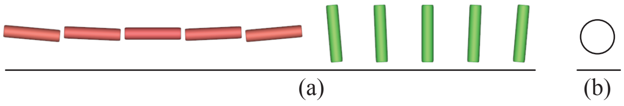
(a) (b)

Figure 3: *(a) A group of linear tensors with two distinct orientations. (b) The Euclidean mean tensor. A mean tensor generated according to Equation (3) would comprise the same scale and shape as the tensors in a) but with a random orientation (thus not shown).*

$p(\mathbf{r})$ is the probability density function of a 3D normal displacement distribution, which is the fundamental assumption underlying DTI. It represents the probability of a water molecule ending up with displacement vector $\mathbf{r}$ after a certain amount of time. dODF is the radial integral of the normal distribution along a given direction $\mathbf{u}$ (i.e., the unit vector). Furthermore, $|\mathbf{D}|$ is the determinant and $\mathbf{D}^{-1}$ is the tensor inverse. The dODF integrates to one over the unit sphere $\mathbb{S}^2$, i.e., $\int_{\mathbb{S}^2} \mathrm{dODF}(\mathbf{u})\, d\mathbf{u} = 1$. It is dimensionless, and invariant with respect to $|\mathbf{D}|$ [ALS*10]. Note that dODF responds to the tensor orientation as well as the tensor shape. The mean dODF, denoted $\overline{\mathrm{dODF}}$, is defined as the average of individual dODFs,

$$\overline{\mathrm{dODF}}(\mathbf{u}) = \frac{1}{n} \sum_{i=1}^{n} \mathrm{dODF}_i(\mathbf{u}). \tag{5}$$

Similar to HARDI, which models multiple diffusion orientations for the case that a single voxel contains multiple fiber orientations (e.g., fiber crossing), the $\overline{\mathrm{dODF}}$ models multiple orientations within the ensemble, and as such provides a faithful representation of the actual diffusion directions. Figure 4a shows the $\overline{\mathrm{dODF}}$ glyph for the tensor ensemble presented in Figure 3a, preserving the two major orientations.

3.2.2. Tensor Ensemble Variations

To quantify the variation in the ensemble separately for scale, shape, and orientation, we generalize the standard deviation σ to the pair-wise tensor difference measures [ZSL*16], denoted as d_{scale}, d_{shape}, and $d_{\mathrm{orientation}}$, respectively. The pair-wise difference measures have several desirable properties, especially in relation to the link between shape and orientation. The orientation difference measure $d_{\mathrm{orientation}}$ is designed to smoothly converge to zero as one of the compared tensors becomes isotropic, ensuring continuity. Furthermore, the difference measures are considerably faster to compute, compared to the *geodesic-loxodromes* approach [KSJEN*07]. Using the pair-wise differences, the standard deviation for each of the intrinsic tensor properties is defined as

$$\sigma_p = \sqrt{\frac{1}{n-1} \sum_{i=1}^{n} \left(d_p\left(\overline{\mathbf{D}}, \mathbf{D}_i\right)\right)^2}, \tag{6}$$

where p is one of the three intrinsic properties {scale, shape, orientation}. The statistical summary contains a mean tensor and three

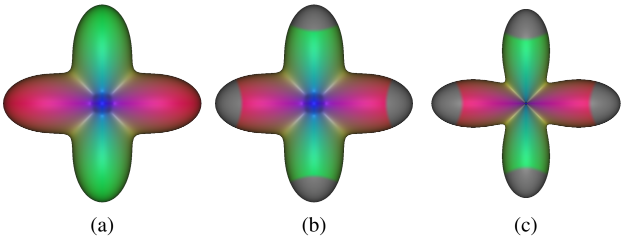
(a) (b) (c)

Figure 4: *(a) The corresponding* $\overline{\mathrm{dODF}}$ *glyph for the tensor ensemble in Figure 3a. A conventional direction-encoded colormap is used. (b) The glyph with the threshold set to 60% of the maximum variation. (c) The glyph of (b) min-max normalized to enhance the direction with a large diffusion probability density.*

scalar-valued quantities that represent the variation within each individual property. Although conceptually similar to the *aggregate covariance measures* proposed by Kindlmann et al. [KEWW07], the {scale, shape, orientation} variations are defined independently of the covariance tensor. Furthermore, since both d_{shape} and $d_{\text{orientation}}$ are bounded [ZSL*16], the corresponding variations σ_{shape} and $\sigma_{\text{orientation}}$ are also bounded.

The standard deviation for dODFs, describing the variation in the diffusion probability density in a given direction $\mathbf{u}$, is then given by

$$\sigma_{\text{dODF}}(\mathbf{u}) = \sqrt{\frac{1}{n-1}\sum_{i=1}^{n}\left(\overline{\text{dODF}}(\mathbf{u}) - \text{dODF}_i(\mathbf{u})\right)^2}. \qquad (7)$$

While conceptually similar to the *variance in Apparent Diffusion Coefficient* (Equation (13) in Abbasloo et al. [AWHS16]), σ_{dODF} provides a direct interpretation compared to the covariance tensor.

Both $\overline{\text{dODF}}$ and σ_{dODF} are functions defined on the unit sphere $\mathbb{S}^2$. Hence, $\overline{\text{dODF}}$ and σ_{dODF} can be approximated with spherical harmonics of up to fourth-order [HMH*06], resulting in two sets of spherical harmonics coefficients per voxel, each containing 15 coefficients. Higher-order approximation would provide more accurate results but at increased computational complexity. For the purpose of numerical computation, an icosahedron-based fourth-order tessellation is employed to discretize $\overline{\text{dODF}}$ and σ_{dODF}.

4. Visual Design Requirement Analysis

Following Shneidermans mantra "Overview first, zoom and filter, then details on demand" [Shn96], we propose a two-level overview + detail visualization. The overview is used to present the aggregate information on the ensemble, presented in Section 3.2. The detail views allow the exploration of the original tensor data.

The goal of the overview visualization is to enable the analyst to inspect the aggregate ensemble information (i.e., mean and variation) at discrete locations in the domain, as well as to reveal potential large-scale coherent patterns. Therefore, we define three requirements for the overview visualization:

O1 It shall show the mean tensor and tensor variations simultaneously in the 3D domain through a single view, to avoid attention shifts and reduce reliance on memory during visual exploration.

O2 The mean and variations in each of the three intrinsic properties should be separable and, therefore, individually identifiable.

O3 When no variation is present in the ensemble, the visual representation shall converge to a well-known base representation, such as a glyph-based visualization for a single DTI dataset, to decrease the entry burden for analysts.

To identify how variations in the ensemble arise and to inspect tensors for different ensemble members, we define the following requirements for the detail visualization:

D1 It shall show the complete tensor ensemble for voxels of interest without assumptions on the ensemble distribution.

D2 It shall allow direct access to the three intrinsic properties separately and facilitate interpretations.

D3 It shall allow to identify correlations between the different intrinsic properties.

5. Glyph-based Overview Visualization

Glyphs principally allow the simultaneous visualization of multiple attributes. Therefore, it is a natural choice to employ glyphs to encode the multivariate summary information (**O1**). Well studied glyph representations (e.g., [Kin04] for DTI, [PPvA*09] for HARDI) form the basis to which our new design should gracefully reduce in case no variation is present in the ensemble (**O3**).

5.1. Tensor-based Glyph Design

Superquadric tensor glyphs are commonly employed as base geometry for their ability to reduce ambiguity and preserve continuity [Kin04, SK10b, SK16]. A glyph G is constructed following

$$G(\mathbf{D}) = s(\text{tr}(\mathbf{D}))\,\mathbf{R}\tilde{\Lambda}B\left(\tilde{\lambda}_j\right), \qquad (8)$$

where the superquadric base geometry $B\left(\tilde{\lambda}_j\right)$ is determined according to the sorted normalized eigenvalues. $\tilde{\Lambda}$ is a diagonal matrix composed of the normalized eigenvalues for scaling the base geometry. $\mathbf{R}$ is a rotation matrix, defined by the column matrix of the eigenvectors $[\mathbf{e}_1, \mathbf{e}_2, \mathbf{e}_3]$. s is an overall scaling function, which takes the tensor trace $\text{tr}(\mathbf{D})$ as input. Unlike the previous work [SK10b, SK16], we can use $\text{tr}(\mathbf{D})$ instead of the Frobenius norm $||\mathbf{D}||$ because we normalize eigenvalues with respect to tensor trace as presented in Section 3.1.

We indicate the major diffusion direction by the conventional spherical colormap [PP99], determined by the absolute values of the components of the major eigenvector $\mathbf{e}_1$. The color is desaturated according to the tensor invariant c_l [WMK*99]. Unless noted otherwise, we use this colormap throughout the paper. In the following, we extend the superquadric glyph to incorporate the tensor variation information based on the fundamental construction rule Equation (8).

Scale Variation. The mapping of data attributes into visual channels of glyphs should be semantic [BKC*13], thus easing the learning process. The influence of the tensor scale on the glyph appearance is reflected in the scaling part $s(\text{tr}(\mathbf{D}))$ of Equation (8). Therefore, we decide to encode the tensor scale variation into glyph halos, similar to [SK10b, ZSL*16]. The larger the scale variation, the thicker is the halo (Figure 5a). Extra benefits brought by halos are the enhancement of depth perception, which is especially important in the context of orthographic projections, and identification of individual glyphs [LKH09]. The halos are generated by rendering the same glyph with a larger scaling factor, by adding the standard deviation to the trace, $s(\text{tr}(\mathbf{D}) + \sigma_{scale})$.

Shape Variation. Shape perception is roughly based on two factors, the underlying geometry, reflected in $\tilde{\Lambda}B\left(\tilde{\lambda}_j\right)$ of Equation (8), and the shading information [War13]. A way to show tensor shape variation would be distorting the geometry and/or shading. However, introducing additional, irregular geometry would lead to a deviation from the commonly used glyphs. Thus it would potentially increase the learning burden. Instead we encode σ_{shape} by introducing a texture on top of the geometry. We propose two different approaches with distinct advantages and disadvantages, and allow the user to select one, depending on the use case.

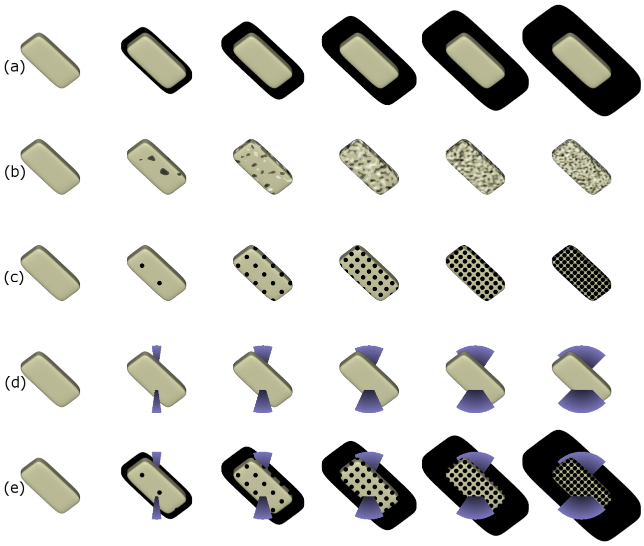

Figure 5: *Visualization of the same mean tensor with different types/extents of variations (a): scale, (b&c): shape with Perline noise and halftone pattern, (d): orientation, (e): all combined. The variation gradually increases from left to right.*

The first approach adds Perlin noise of increasing frequency to indicate increasing σ_{shape} in object space, similar to previous work [BWE05, HdMRHH16], as shown in Figure 5b. Glyphs encoding large variations will show strong luminance contrast, to which the human visual system is sensitive [War13]. The resulting texture will be invisible for $\sigma_{shape} = 0$ and, therefore, resembles the appearance of the glyph for a single dataset. The second approach employs a screen-space halftone pattern [SLK*17], as shown in Figure 5c. Here, σ_{shape} is encoded into the distances between neighboring dots on the glyph surface. The distance is inversely proportional to σ_{shape}. Smaller variations result in much larger distances while higher variations result in more densely packed dots.

The halftone pattern provides a more precise estimation of tensor shape variations, however, at the expense of artifacts during interaction, due to its screen space nature. The Perlin noise does not suffer from these artifacts, but is harder to interpret and quantify due to its irregularity. A downside for both techniques is their interference with color, which means that properties encoded by the color (e.g., the major eigenvector or FA) will become less legible.

Orientation Variation. The orientation information is reflected in the rotation matrix **R** of Equation (8). One option to visualize $\sigma_{orientation}$ is to superimpose several glyphs with perturbed rotations [JGA*02]. However, this is likely to cause strong occlusions. Instead, we explicitly show $\sigma_{orientation}$ with a sector as shown in Figure 5d. Since there is no inherent orientation for the 2D sectors in the 3D domain, we align them with the view direction [LKH09] to maintain optimal visibility. The orientation variation $\sigma_{orientation}$ is then encoded into the angle of the sector by the same mapping function as introduced in our previous work [ZSL*16], with larger sectors indicating larger $\sigma_{orientation}$.

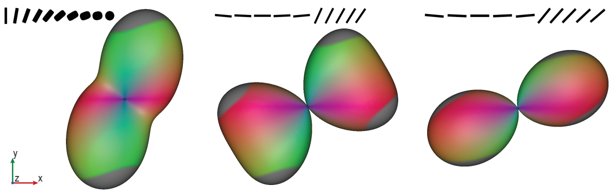

(a) (b) (c)

Figure 6: *Three dODF-based glyphs for (a) an ensemble with gradually varying shape and orientation and two ensembles of linear tensors with crossing angle of (b)* 60 ° *and (c)* 45 °*, respectively. The variation threshold is set to 60% of the maximum variation. The ensembles are illustrated by the small black icons on top.*

As shown in Figure 5, the halo, the surface texture, and the sector, visually encoding tensor variations in scale, shape, and orientation, respectively, are individually recognizable (**O2**). Furthermore, our design converges to the original superquadric glyph representation when no variation is present (**O3**, left column of Figure 5).

5.2. dODF-based Glyph Design

We use the conventional spherical plot, which is commonly used to visualize HARDI data [PPvA*09], to visualize $\overline{\text{dODF}}$. The glyph geometry represents the average diffusion probability density for each direction. Additionally, to emphasize the directional information, the *de facto* direction-coded colormap is used. This colormap can influence the shape perception [BT07], however, it is familiar to the the target users. In order to incorporate the variation information, we employ a threshold-based method. Directional variation is encoded into neutral gray if it is greater than the user-specified threshold. We choose a neutral gray, with lightness value 0.5 in the CIE Lab color space, which has similar lightness as, but is not part of the direction-coded colormap to minimize the interference with the perception of the directional and shape information. Figure 4b shows the dODF glyph with the variations incorporated, derived from the ensemble of linear tensors in Figure 3a. This representation preserves the two major diffusion orientations that are present in the ensemble and the large variation is visible at the four lobes. Moreover, min-max normalization [PPvA*09] is used to enhance the visual perception of directional maxima (e.g., see Figure 4c). The extended dODF glyph meets the requirements **O2** and **O3**. Figure 6 further illustrates the dODF glyph representation for three different ensembles.

5.3. Spatial Overview

To fulfill requirement **O1**, glyphs are laid out according to their location in the data in a spatial view. We construct the tensor glyph (Section 5.1) and the dODF glyph (Section 5.2) for each voxel. Displaying both simultaneously would result in occlusion and visual clutter. Therefore, we show only a single, user selected glyph type at a time. The distinct properties of the two glyphs make them suitable for different tasks. If the analyst is interested in variations in individual tensor properties, the tensor glyph is the best choice; for detailed information on the orientation variation the dODF glyph is more suitable.

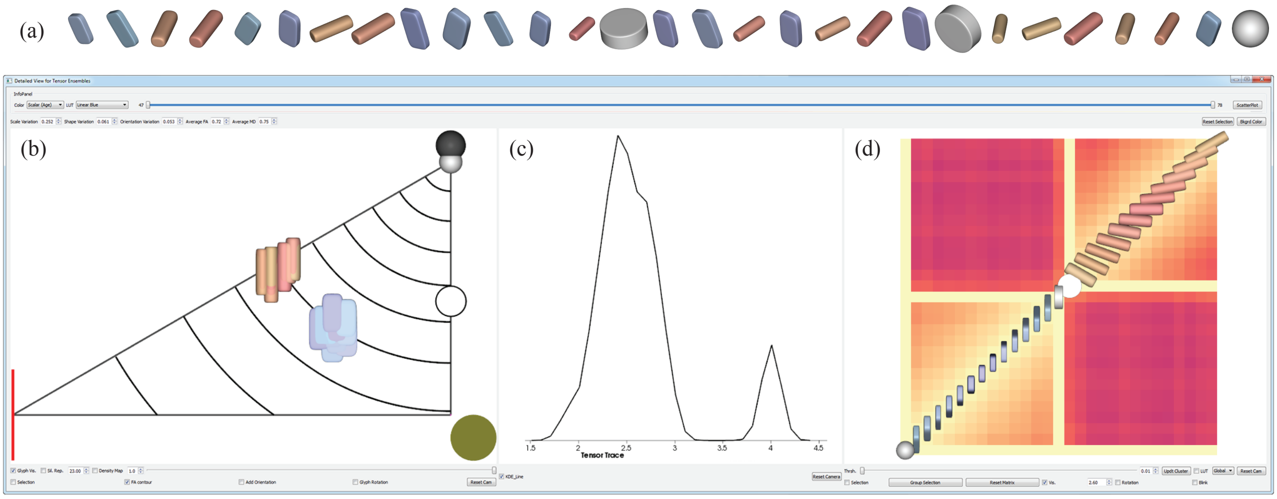

Detailed View for Tensor Ensembles
InfoPanel
Color Scalar (Age) LUT Linear Blue 47 78
Scale Variation 0.252 Shape Variation 0.061 Orientation Variation 0.053 Average FA 0.72 Average MD 0.75
☑ Glyph Vis. ☐ Sil. Rep. 23.00 ☐ Density Map 1.0
☐ Selection ☑ FA contour ☐ Add Orientation ☐ Glyph Rotation
☑ KDE_Line
Thrsh. 0.01 ☐ LUT Global
☐ Selection ☑ Vis. 2.60 ☐ Rotation ☐ Blink

Figure 7: *Our framework for the linked detail views. (a) shows a direct visualization of a synthetic set of tensors containing one isotropic tensor and two planar-anisotropic tensors, similar to small multiples. (b) shows the shape space view, (c) the scale space view, and (d) the orientation dissimilarity matrix view with a perceptually linear magma colormap for all the tensors in (a).*

6. Detail Visualization

Based on the overview glyphs, the analyst can identify regions of interest and select few individual voxels for detail inspection of the ensemble. For further inspection of selected voxels, we provide linked detail views. A straightforward way to display all tensors (**D1**) within the ensemble are small multiples. However, simply placing the glyphs next to each, e.g. ordered by their id in the ensemble, hardly brings usable insights, as shown in Figure 7a. For effective comparison, data visualized as small multiples need to be ordered. Due to their multivariate nature, however, the tensor glyphs presented above have no intrinsic order, and imposing an arbitrary order violates the *representation invariance principle* [KS14]. Following the idea of separating the intrinsic properties, we propose to show scale, shape, and orientation in three linked views, as shown in Figure 7. The separation fulfills **D2**. Furthermore, linking these views fulfills **D3**. To facilitate quantitative analysis, we also display all the statistical information (e.g., σ_{shape}) via graphical user interfaces.

6.1. Tensor Scale Visualization

Visualizing the scalar-valued tensor scale is straightforward. We estimate the probability density function of the tensor scales within the ensemble using a 1D kernel density estimate. The function is visualized directly in a 1D line plot. The exemplary plot in Figure 7c clearly shows the distribution of scale within the ensemble in Figure 7a.

6.2. Tensor Shape Space Visualization

Figure 7b shows the proposed shape space visualization using the ensemble presented in Figure 7a. The tensor shape space is two dimensional and maps to a right triangle in $\mathbb{R}^3$ in Figure 2. We show the triangle in the background and draw the three interpretable extreme glyphs on the corners of the triangle. Additionally we show the iso-contours of other tensor invariants (e.g., FA) for contextual information, as the curved lines shown in Figure 7b. In principal the shape space visualization is a scatterplot. However, a mental reconstruction of the actual shape, just from the position and the extreme glyphs, is challenging. Therefore, we show the glyphs with unit scale and identical orientation to represent the tensor shape information in the plot. To reduce clutter, the size of the glyphs is adjustable. In the smallest setting, the shape space visualization becomes a standard scatterplot. Finally, the color channel is left for encoding additional information such as the age of the individuals.

6.3. Orientation Dissimilarity Matrix Visualization

The tensor orientation, given by the rotation matrix $[\mathbf{e}_1, \mathbf{e}_2, \mathbf{e}_3]$, is an element of the manifold of the group SO(3), and as such, has three dimensions. However, if a tensor has equal eigenvalues its eigenvectors are ill-defined. For example, the orientation of an isotropic tensor is undefined. Due to this coupling of shape and orientation, it is not straightforward to define a space to show the distribution of tensor orientations. To sidestep this problem, we propose to compute pair-wise differences of the orientation using $d_{\text{orientation}}$ [ZSL*16]. We visualize the pair-wise differences as a dissimilarity matrix, as shown in Figure 7d, which would allow us to identify patterns in the orientation behavior. A good ordering is essential to identify clusters of tensors with similar orientations. Thus we arrange the rows and columns of the matrix view using hierarchical clustering [BBHR*16].

The orientation difference measure $d_{\text{orientation}}$ is not a *metric*. For example, a planar tensor has no orientation difference with any tensor that has the same minor eigenvector $\mathbf{e}_3$. We refer to such a tensor $\mathbf{D}^{oc}$, where $d_{\text{orientation}}(\mathbf{D}^{oc}, \mathbf{D}_i) = 0$ for $i = 1 \ldots n$, as an *oricentric* tensor. Considering the orientation differences $d_{\text{orientation}}$

only, oricentric tensors have no inherent order and, hence, can be placed at random positions during ordered hierarchical clustering [GW72]. Therefore, we propose a custom, *top-down* hierarchical clustering approach. We first divide the ensemble into oricentric and non-oricentric tensors. The oricentric tensors are clustered according to d_{shape}, which is a metric, using hierarchical clustering with complete-linkage. The group of non-oricentric tensors is then bisected, using the k-medoids algorithm [KR87] with $k = 2$, based on $d_{\text{orientation}}$. The bisection can cause tensors that were non-oricentric in relation to the complete ensemble to be oricentric in relation to the new subsets. Therefore, we recursively apply the separation into non-oricentric and oricentric subsets, followed by the bisection of the non-oricentric subset, until non-oricentric subset contains at most one or two tensors.

As suggested by Gruvae and Wainer [GW72], we concatenate two subsets such that elements on the edge of different subsets that are most similar are placed next to each other to show the relation between subsets. To concatenate two non-oricentric subsets, we choose the pair of edge elements with the smallest orientation difference while for a non-oricentric subset and an oricentric subset, we choose the pair with the smallest shape difference.

6.4. Linked Brushing

Each of the three views presents only one aspect of the tensor properties in the ensemble. We use linked brushing to connect all the three views and to reveal correlations between different tensor properties (**D3**). Therefore, we propagate selections defined in one view to the other linked views. Thus, all the selected tensors in all the three views will be red highlighted. We also provide the option to render only the silhouettes of glyphs that are not selected in order to reduce occlusions.

7. Implementation

Our prototype is implemented in `C++`, combining `VTK` and `OpenGL/GLSL` for visualization. We use `Qt` for the GUI and `Teem` (`teem.sourceforge.net`) for tensor data processing.

The glyph rendering is implemented by computing base geometries and storing them in GPU memory, as proposed by Schultz and Kindlmann [SK10b]. We use three renderpasses to render the glyphs and corresponding variation information. In the first pass we draw the mean tensor glyph, including the texture indicating the shape variation. We linearly scale $[0, \sigma_{shape}]$ to $[0, 1]$. Since the theoretical maximum of tensor shape difference d_{shape} is $\sqrt{2/3}$, which corresponds to the length of the hypotenuse of the right triangle in Figure 2, typical σ_{shape} values are significantly smaller than 1 and therefore require the scaling. We render the Perlin noise texture by first assigning a random value *rand* between -1.0 and 1.0 to every fragment, with the fragments' object space coordinates and σ_{shape} as the input for the Perlin noise generator. To guarantee that the color-encoded information is legible to some extent, we only apply the texture to fragments with $|rand| < (1 - \sigma_{shape})$. We darken the fragments with negative sign while we brighten those with positive sign. We then render the halos by redrawing the geometry with increased size in black in the second pass, and finally the sectors in the third pass.

The dODF-based glyphs are rendered via ray casting [PPvA*09]. After determining the intersection point $\mathbf{p}$ of the ray with the glyph, we use the unit directional vector, $\mathbf{u} = \mathbf{v}/\|\mathbf{v}\|$ with $\mathbf{v} = \mathbf{p} - \mathbf{c}_{\text{glyph}}$ and the glyph center $\mathbf{c}_{\text{glyph}}$, to compute the diffusion probability density variation according to Equation 7.

8. Evaluation and Application

In this section, we compare our design to the work of Abbasloo et. al. [AWHS16], which is the closest to our work. We consider that domain knowledge is essential to understand the presented visual analysis. Unfortunately, this limits the number of possible participants. Here, we present a qualitative user study with two neuroscientists. We also present a case study illustrating the potential of our prototype with a real-world ensemble of 46 DTI datasets.

8.1. Method Comparison

Abbasloo et al. [AWHS16] use small multiples for the six eigenmodes, $\mathbf{E}^k$ with $k = 1, \ldots, 6$, of the fourth-order covariance tensor. To illustrate the effects of each eigenmode, they build a pair of tensors $\mathbf{D}(t;k) = \mathbf{D}^{\text{Eu}} \pm t\mu_k \mathbf{E}^k$, where $\mathbf{D}^{\text{Eu}}$ is the Euclidean mean tensor and μ_k is the square root of the corresponding eigenvalues of the covariance tensor. The parameter t can be freely adjusted by users. The pair of tensors is then rendered with two complementary colors, blue and orange. The normalized covariance tensor is decomposed with respect to the spherical invariants set (i.e., Frobenius norm, FA, and tensor mode) and rotation tangents [KEWW07],

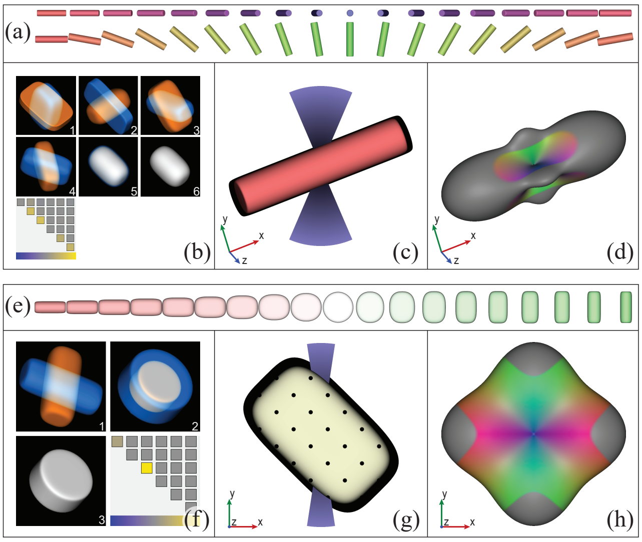

Figure 8: *Comparison of two different aggregate visualizations for two different synthetic ensembles ((a) and (e)). (b) and (f) show the glyph-based eigenmodes visualization and IGRT matrix view. (c) and (g) show our tensor glyphs, depicting the variations in instinct properties. (d) and (h) show the dODF-based glyphs. The direction with large variations are colored in gray. For the purpose of clear illustration, images are generated from different viewpoints.*

and displayed via a blue-gray-yellow colormap. Figures 8b and 8f show their visualizations. Figures 8c and 8g show our tensor glyphs while Figures 8d and 8h show our dODF-based glyphs. The variation threshold of $\overline{\text{dODF}}$ can be freely adjusted by users as well.

During the experiment, we first gave an introduction with a live demo of the two visualizations to be compared and the corresponding interaction methods. At this time, the participants interacted with the prototype to get themselves familiar with the visualizations. The objects of comparison are the aggregated glyphs in Section 5 and the visualizations proposed by Abbasloo et al. [AWHS16] of three synthetic datasets. We presented them to the participants, together with interaction capabilities, in *random* order. The participants freely analyzed the visualizations, and then we asked them to describe the original ensemble based on the aggregated visualizations they were observing in the form of a questionnaire. The participants had *no* information on the configuration of the ensembles apart from the provided aggregated visualizations, beforehand.

The first ensemble in Figure 8a comprises most variation in the orientation, some variation in scale, and no variation in shape. The scale variation is captured by all visual representations as suggested by the fourth eigenmode in Figure 8b and the visible halo in Figure 8c, respectively. The IGRT (i.e., invariant gradients and rotation tangents [KEWW07]) matrix of Abbasloo et al. shows high values in the 2nd and 3rd diagonal entries, corresponding to FA and mode respectively. The first and second eigenmodes, shown in the small multiples of Figure 8b, however, falsely indicates variation in shape. Our tensor glyph in Figure 8c shows no variation in shape. Both participants could not describe the variation in tensor shapes using the method of Abbasloo et al., while with our visualization they readily confirmed that only linear tensors are included in the ensemble. In Abbasloo et al., the third and fourth eigenmodes, together with the rotation tangents part of the IGRT matrix, i.e., the bottom three diagonal entries, show orientation variation in two orthogonal directions. The first and second eigenmodes show clear simultaneous variation in orientation and shape. One participant commented that it is really hard for him to combine all the eigenmodes to deduce information about the ensemble. Both participants deliberately ignored the rotations manifested in the first and second eigenmodes in Figure 8b when deducing the orientation, and came to the correct conclusion that there are two main directions of rotation in the ensemble. Our aggregated tensor glyph in Figure 8c makes the orientation variation directly visible as a large sector. Furthermore, the dODFglyph in Figure 8d shows the principle diffusion direction as three orthogonal directions with high diffusion variation. Combining both glyphs, they came to the conclusion that a group of linear tensors spreads around the major eigenvector $\mathbf{e}_1$ of the mean tensor, which, while not describing the orientation variation exactly, is very close to the correct description.

The second ensemble in Figure 8e shows some variation in scale, shape, and orientation. This simulates the interface between two orthogonally aligned fiber tracts [KEWW07]. In Abbasloo et al., the last four eigenmodes correspond to zero eigenvalues. Therefore, we only keep the first three views in Figure 8f. The orientation and scale variation are manifested in the first and second eigenmode, respectively. The IGRT matrix in Figure 8f, however, indicates no variation in orientation (see the bottom three rows) but large variation in tensor mode (see the 3rd diagonal entry), which is part of the tensor shape. This contradiction between the eigenmode views and the IGRT matrix view causes considerable confusion for both participants. This is caused by the fact the variation in mode and minor eigenvector, shown as the 3rd and 6th diagonal entries respectively, should be interpreted integrally [KEWW07] near a planar mean tensor. Our tensor glyph in Figure 8g shows variation for all the three properties. The dODF glyph in Figure 8h provides additional information, indicating two main orthogonal directions with high diffusion variation. Both participants speculated that there may be fiber crossing effects in the underlying ensemble.

After the participants finished the overview analysis we showed them the underlying ensemble with our detail views and informally discussed the application. With regard to the tensor scale, the visualization of Abbasloo et al. and ours work well. However, our technique is found to be more accurately describing the shapes in the ensemble. In terms of tensor orientation, both participants remarked that the non-linearity of tensor orientations makes the covariance-based visualization harder to understand. With our method they could readily identify orientation variation but both thought it requires a considerable learning curve to interpret the dODF and to effectively combine the information of the two aggregated glyphs. Another insight we learn from the user study is that the visual representation of the shape variation is not optimal. While participants found the noise texture less readable than the half tone texture, they preferred the stability of the object-space Perlin noise. We intend to explore other visual design idioms to optimize this in the future.

We do not show correlations between different tensor properties explicitly in our glyph designs. Correlations can be shown via eigenmodes, and the off-diagonal entries of the IGRT matrix. However, it is unclear whether it can be reliably interpreted. For instance, the first and second eigenmodes in Figure 8b indicate some relation in shape and orientation but there is no shape variation in the ensemble. Generally, both participants deem the proposed mean tensor, based on the separation of tensor intrinsic properties, as well as our visual design more intuitive.

8.2. Application to DTI Ensembles of Healthy Subjects

In this section, we present an exemplary analysis of a cohort DTI study, conducted with a neuroscientist, who is specialized in DTI-based group analysis and a co-author of this paper. The dataset used for this case study is an ensemble, consisting of 46 DTI scans of healthy volunteers, age 47 to 78, serving as the control group in clinical research. Each scan has a resolution of $224 \times 224 \times 144$ with isotropic voxel size of 2mm. The diffusion weighting is b$=$ $1000\,\mathrm{s/mm^2}$ along 64 uniformly distributed directions with four non-diffusion averages. The numerical range of the tensor values is scaled by 1000. The datasets are registered with a non-rigid registration approach by DTI-TK, which takes the whole tensor information into consideration [ZYAG06].

During the visual exploration with the glyph-based overview in Figure 9b, we find a region of interest (ROI) with both high scale and shape variations. This region (see green highlight in Figure 9a) corresponds to the border between the ventricle, corpus

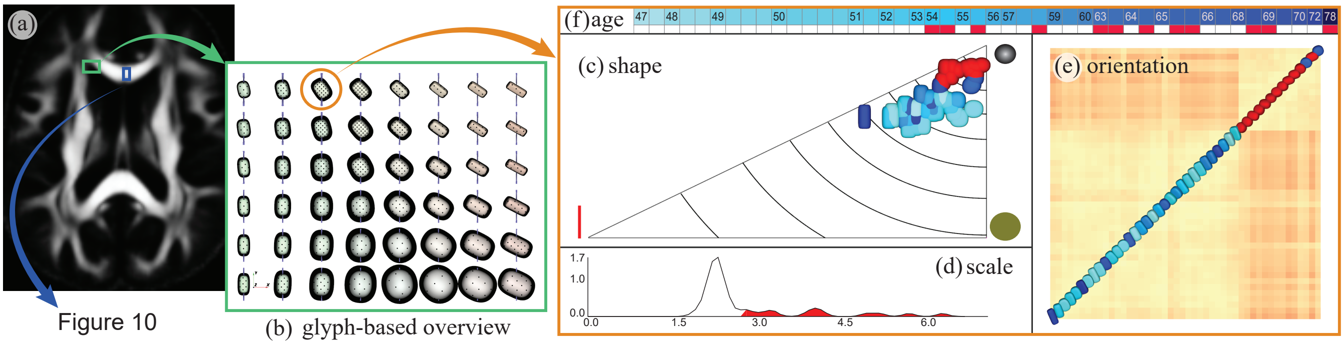

Figure 9: *Visual analysis results for a border region of ventricle, CC, and IFO (a). The glyph-based overview (b) guides the selection of a voxel of interest for further exploration via shape space (c), scale line plot (d), orientation difference matrix (e), and age information (f).*

callosum (CC), and inferior fronto-occipital fasciculus (IFO). The glyph-based overview in Figure 9b shows small variation in orientation (i.e., small sector angle). The glyphs in the bottom-right have thicker halos, indicating a larger scale variation, compared to the glyphs corresponding to the fibrous regions, i.e., bright areas in Figure 9a. In contrast, shape variation shown as half tone patterns is stronger in the top region. We now make a selection and use the detail views for further exploration. We select one of the voxels with larger shape and scale variation (see orange highlight in Figure 9b). In the detail views, the glyph color encodes the subject age. In the shape space view in Figure 9c, we see a transition from anisotropic tensors to nearly isotropic tensors. The scale view in Figure 9d shows a right-skewed distribution with a strong peak at lower scale values, as well as several large values. Selecting the right tail of the distribution in the scale view reveals the nearly isotropic tensors in the shape-space view via linked brushing, i.e., red highlighted in the different detail views. We also highlight the selection in a simple table view in Figure 9f, clearly identifying the older subjects. This confirms the expectation that older people have larger ventricles [RPK*03, LGC*12], resulting in tensors with lower diffusion anisotropies but high diffusion scales. Somewhat unexpected is a clear separation in the orientation view in Figure 9e, even though differences in orientation are generally small, as already indicated by the glyph-based overview. Interestingly, there seems to be further correlation with age, placing the previously selected tensors all in one group on the top right of the diagonal.

For the second analysis, we choose a different ROI (see blue highlight in Figure 9a) in the CC to illustrate that our detail views can be used to identify potential outliers. The glyph-based overview in Figure 10a shows that the variations in the ensemble are similar throughout the selected region. Slight variation in orientation and some variation in scale and shape can be identified. We select a voxel in the center, highlighted in Figure 10a, for further inspection in the detail views. An outlier tensor with lower anisotropy, encircled in Figure 10b top, becomes apparent. Through the linked selection we also find this member exhibits a larger scale value (see the encirclement in Figure 10c top) compared to the rest of the ensemble members. To verify that this behavior is consistent in the complete ROI, we select the 18 voxels in Figure 10a for visualization in the shape space view (Figure 10b bottom). We now select the subject corresponding to the outlier, identified in Figure 10b top, through the table view, highlighting only the corresponding tensors in the shape space view in Figure 10b bottom. The selection highlight clearly shows that all the corresponding diffusion tensors have coherently lower anisotropies (see Figure 10b bottom) and generally larger scale values (see Figure 10c bottom). This indicates that the selected ensemble member as a whole could be regarded as an outlier for this area.

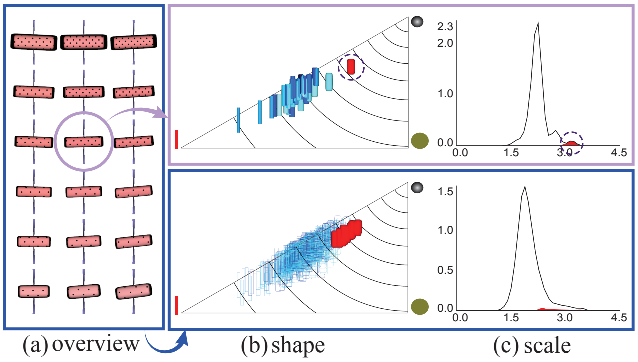

Figure 10: *Identification of potential outliers in a region of the corpus callosum, highlighted in blue in Figure 9a. (a) shows the overview glyph visualization. (b) and (c) show the shape space view and scale line plot for (top) the selected voxel in (a) and (bottom) the complete ROI, respectively.*

9. Discussion and Conclusion

We present an interactive approach for the analysis, visualization, and exploration of diffusion tensor ensembles. At the core of our visual analysis approach is a novel way to compute a representative tensor and quantify tensor variation through tensor intrinsic properties (i.e., scale, shape, and orientation), each of which has a biologically meaningful interpretation. By adapting the dODF, we provide an alternative for aggregating orientation variation, for cases where a single representative tensor cannot properly summarize different orientations in the ensemble. Another core contribution is the overview + detail visual design to facilitate per-voxel inspection of variation of tensor intrinsic properties free of assumptions about the underlying distribution. Finally, we demonstrate the effectiveness of our approach by comparing it to previous work by means of a qualitative user study with two domain experts and show the potential of our design by a case study.

The conducted user study requires knowledge about diffusion tensor analysis as well as multilinear normal distributions and as such limits the pool of possible participants. We consider a larger user study that would allow for strong conclusions on the effectiveness of the presented techniques future work.

We test our detail view system for ensembles of less than hundred members, a reasonable number for current DTI group studies. However, scaling to much larger numbers of ensemble members would require other solutions, specifically with respect to the visualizations of tensor shape space and orientation difference matrix.

Apart from data aggregation, another main task when conducting DTI group studies is the detection of potential outliers. While we demonstrate outlier detection using our detail views, our glyph representation currently does not provide any information on potential outliers. To ease the process of outlier detection a careful adaption of the glyph design that does not increase clutter is needed.

Finally, our design is targeted at second-order positive-definite tensors. However, similar rules apply to the glyph construction of second-order symmetric tensors [SK10b]. Investigating the applicability of our design to those or even general second-order tensors would be an interesting future direction.

Acknowledgements

We gratefully acknowledge the Co-morbidity in relation to Aids (COBRA) project and specifically Dr. James Cole (Department of Medicine, Imperial College London) for providing the DTI ensemble that is used in Section 8.2. We would like to thank the authors of [AWHS16] for providing their source code, and the anonymous reviewers for their constructive comments.

References

[ALS*10] Aganj I., Lenglet C., Sapiro G., Yacoub E., Ugurbil K., Harel N.: Reconstruction of the orientation distribution function in single- and multiple-shell q-ball imaging within constant solid angle. *Magnetic Resonance in Medicine 64*, 2 (2010), 554–566. 4

[AWHS16] Abbasloo A., Wiens V., Hermann M., Schultz T.: Visualizing tensor normal distributions at multiple levels of detail. *IEEE Transactions on Visualization and Computer Graphics 22*, 1 (2016), 975–984. 1, 2, 3, 5, 8, 9, 11

[BBHR*16] Behrisch M., Bach B., Henry Riche N., Schreck T., Fekete J.-D.: Matrix reordering methods for table and network visualization. *Computer Graphics Forum 35*, 3 (2016), 693–716. 7

[BHJ*14] Bonneau G.-P., Hege H.-C., Johnson C. R., Oliveira M. M., Potter K., Rheingans P., Schultz T.: Overview and state-of-the-art of uncertainty visualization. In *Scientific Visualization: Uncertainty, Multifield, Biomedical, and Scalable Visualization*. 2014, pp. 3–27. 2

[BKC*13] Borgo R., Kehrer J., Chung D. H. S., Maguire E., Laramee R. S., Hauser H., Ward M., Chen M.: Glyph-based visualization: Foundations, design guidelines, techniques and applications. In *Eurographics State of the Art Reports* (2013), pp. 39–63. 5

[BML94] Basser P., Mattiello J., LeBihan D.: MR diffusion tensor spectroscopy and imaging. *Biophysical Journal 66*, 1 (1994), 259–267. 1

[BP96] Basser P. J., Pierpaoli C.: Microstructural and physiological features of tissues elucidated by quantitative-diffusion-tensor MRI. *Journal of Magnetic Resonance 111*, 3 (1996), 209–219. 1, 3

[BP03] Basser P. J., Pajevic S.: A normal distribution for tensor-valued random variables: applications to diffusion tensor MRI. *IEEE Transactions on Medical Imaging 22*, 7 (2003), 785–794. 1, 2, 3

[BP07] Basser P., Pajevic S.: Spectral decomposition of a 4th-order covariance tensor: applications to diffusion tensor MRI. *Signal Processing 87*, 2 (2007), 220–236. 1, 2

[BT07] Borland D., Taylor II R. M.: Rainbow color map (still) considered harmful. *IEEE Computer Graphics and Applications 27*, 2 (2007), 14–17. 6

[BWE05] Botchen R. P., Weiskopf D., Ertl T.: Texture-based visualization of uncertainty in flow fields. In *IEEE Visualization* (2005), pp. 647–654. 2, 6

[DJB*11] Douaud G., Jbabdi S., Behrens T. E., Menke R. A., Gass A., Monsch A. U., Rao A., Whitcher B., Kindlmann G., Matthews P. M., Smith S.: DTI measures in crossing-fibre areas: Increased diffusion anisotropy reveals early white matter alteration in MCI and mild Alzheimer's disease. *NeuroImage 55*, 3 (2011), 880–890. 1

[DKLP01] Djurcilov S., Kim K., Lermusiaux P. F. J., Pang A.: Volume rendering data with uncertainty information. In *Joint Eurographics / IEEE TCVG Symposium on Visualization* (2001), pp. 243–252. 2

[EK06] Ennis D. B., Kindlmann G.: Orthogonal tensor invariants and the analysis of diffusion tensor magnetic resonance images. *Magnetic Resonance in Medicine 55*, 1 (2006), 136–146. 3

[FBW16] Ferstl F., BÃijrger K., Westermann R.: Streamline variability plots for characterizing the uncertainty in vector field ensembles. *IEEE Transactions on Visualization and Computer Graphics 22*, 1 (2016), 767–776. 2

[GW72] Gruvaeus G., Wainer H.: Two additions to hierarchical cluster analysis. *British Journal of Mathematical and Statistical Psychology 25*, 2 (1972), 200–206. 8

[GWK*12] Gahm J. K., Wisniewski N., Kindlmann G., Kung G. L., Klug W. S., Garfinkel A., Ennis D. B.: Linear invariant tensor interpolation applied to cardiac diffusion tensor MRI. In *MICCAI*. 2012, pp. 494–501. 3

[HdMRHH16] Höllt T., de Matos Ravanelli F., Hadwiger M., Hoteit I.: Visual analysis of reservoir simulation ensembles. In *Workshop on Visualization in Environmental Sciences* (2016), pp. 1–4. 6

[HLNW11] Hlawatsch M., Leube P., Nowak W., Weiskopf D.: Flow radar glyphs-static visualization of unsteady flow with uncertainty. *IEEE Transactions on Visualization and Computer Graphics 17*, 12 (2011), 1949–1958. 2

[HMH*06] Hess C. P., Mukherjee P., Han E. T., Xu D., Vigneron D. B.: Q-ball reconstruction of multimodal fiber orientations using the spherical harmonic basis. *Magnetic Resonance in Medicine 56*, 1 (2006), 104–117. 5

[HMZ*14] Höllt T., Magdy A., Zhan P., Chen G., Gopalakrishnan G., Hoteit I., Hansen C. D., Hadwiger M.: Ovis: A framework for visual analysis of ocean forecast ensembles. *IEEE Transactions on Visualization and Computer Graphics 20*, 8 (2014), 1114–1126. 2

[JDKW15] Jarema M., Demir I., Kehrer J., Westermann R.: Comparative visual analysis of vector field ensembles. In *IEEE Conference on Visual Analytics Science and Technology* (2015), pp. 81–88. 2

[JGA*02] Jones D. K., Griffin L. D., Alexander D. C., Catani

M., Horsfield M. A., Howard R., Williams S. C.: Spatial normalization and averaging of diffusion tensor MRI data sets. *NeuroImage 17*, 2 (2002), 592–617. 2, 6

[JPGJ12] Jiao F., Phillips J. M., Gur Y., Johnson C. R.: Uncertainty visualization in HARDI based on ensembles of odfs. In *IEEE Pacific Visualization Symposium* (2012), pp. 193–200. 2

[KEWW07] Kindlmann G., Ennis D. B., Whitaker R. T., Westin C. F.: Diffusion tensor analysis with invariant gradients and rotation tangents. *IEEE Transactions on Medical Imaging 26*, 11 (2007), 1483–1499. 2, 5, 8, 9

[Kin04] Kindlmann G.: Superquadric tensor glyphs. In *Joint Eurographics / IEEE TCVG Symposium on Visualization* (2004), pp. 147–154. 1, 2, 5

[KR87] Kaufmann L., Rousseeuw P.: Clustering by means of medoids. *Statistical Data Analysis Based on the L1-Norm and Related Methods* (1987), 405–416. 8

[KS14] Kindlmann G., Scheidegger C.: An algebraic process for visualization design. *IEEE Transactions on Visualization and Computer Graphics 20*, 12 (2014), 2181–2190. 7

[KSJEN*07] Kindlmann G., San José Estépar R., Niethammer M., Haker S., Westin C.-F.: Geodesic-loxodromes for diffusion tensor interpolation and difference measurement. In *MICCAI*. 2007, pp. 1–9. 3, 4

[LGC*12] Lebel C., Gee M., Camicioli R., Wieler M., Martin W., Beaulieu C.: Diffusion tensor imaging of white matter tract evolution over the lifespan. *NeuroImage 60*, 1 (2012), 340–352. 10

[LKH09] Lie A. E., Kehrer J., Hauser H.: Critical design and realization aspects of glyph-based 3D data visualization. In *Spring Conference on Computer Graphics* (2009), pp. 19–26. 5, 6

[LPK05] Love A. L., Pang A., Kao D. L.: Visualizing spatial multivalue data. *IEEE Computer Graphics and Applications 25*, 3 (2005), 69–79. 2

[MBW*11] Menzler K., Belke M., Wehrmann E., Krakow K., Lengler U., Jansen A., Hamer H., Oertel W., Rosenow F., Knake S.: Men and women are different: Diffusion tensor imaging reveals sexual dimorphism in the microstructure of the thalamus, corpus callosum and cingulum. *NeuroImage 54*, 4 (2011), 2557 – 2562. 1

[MVB*17] Meuschke M., Voss S., Beuing O., Preim B., Lawonn K.: Glyph-based comparative stress tensor visualization in cerebral aneurysms. *Computer Graphics Forum 36*, 3 (2017), in press. 2

[MWK14] Mirzargar M., Whitaker R. T., Kirby R. M.: Curve boxplot: Generalization of boxplot for ensembles of curves. *IEEE Transactions on Visualization and Computer Graphics 20*, 12 (2014), 2654–2663. 2

[OGT11] Otto M., Germer T., Theisel H.: Uncertain topology of 3D vector fields. In *IEEE Pacific Visualization Symposium* (2011), pp. 67–74. 2

[PB96] Pierpaoli C., Basser P. J.: Toward a quantitative assessment of diffusion anisotropy. *Magnetic Resonance in Medicine 36*, 6 (1996), 893–906. 2

[PH11] Pöthkow K., Hege H.-C.: Positional uncertainty of isocontours: Condition analysis and probabilistic measures. *IEEE Transactions on Visualization and Computer Graphics 17*, 10 (2011), 1393–1406. 2

[PKRJ10] Potter K., Kniss J., Riesenfeld R., Johnson C.: Visualizing summary statistics and uncertainty. *Computer Graphics Forum 29*, 3 (2010), 823–832. 2

[PMW13] Pfaffelmoser T., Mihai M., Westermann R.: Visualizing the variability of gradients in uncertain 2D scalar fields. *IEEE Transactions on Visualization and Computer Graphics 19*, 11 (2013), 1948–1961. 2

[PP99] Pajevic S., Pierpaoli C.: Color schemes to represent the orientation of anisotropic tissues from diffusion tensor data: Application to white matter fiber tract mapping in the human brain. *Magnetic Resonance in Medicine 42*, 3 (1999), 526–540. 5

[PPvA*09] Peeters T. H. J. M., Prckovska V., van Almsick M., Vilanova A., ter Haar Romeny B. M.: Fast and sleek glyph rendering for interactive HARDI data exploration. In *IEEE Pacific Visualization Symposium* (2009), pp. 153–160. 1, 2, 5, 6, 8

[PRW11] Pfaffelmoser T., Reitinger M., Westermann R.: Visualizing the positional and geometrical variability of isosurfaces in uncertain scalar fields. *Computer Graphics Forum 30*, 3 (2011), 951–960. 2

[PWB*09] Potter K., Wilson A., Bremer P. T., Williams D., Doutriaux C., Pascucci V., Johnson C. R.: Ensemble-vis: A framework for the statistical visualization of ensemble data. In *IEEE International Conference on Data Mining Workshops* (2009), pp. 233–240. 2

[PWH11] Pöthkow K., Weber B., Hege H.-C.: Probabilistic marching cubes. *Computer Graphics Forum 30*, 3 (2011), 931–940. 2

[RPK*03] Resnick S. M., Pham D. L., Kraut M. A., Zonderman A. B., Davatzikos C.: Longitudinal magnetic resonance imaging studies of older adults: A shrinking brain. *The Journal of Neuroscience 23*, 8 (2003), 3295–3301. 10

[Shn96] Shneiderman B.: The eyes have it: A task by data type taxonomy for information visualizations. In *IEEE Symposium on Visual Languages* (1996), pp. 336–343. 5

[SK10a] Schultz T., Kindlmann G.: A maximum enhancing higher-order tensor glyph. *Computer Graphics Forum 29*, 3 (2010), 1143–1152. 2

[SK10b] Schultz T., Kindlmann G. L.: Superquadric glyphs for symmetric second-order tensors. *IEEE Transactions on Visualization and Computer Graphics 16*, 6 (2010), 1595–1604. 5, 8, 11

[SK16] Seltzer N., Kindlmann G.: Glyphs for asymmetric second-order 2D tensors. *Computer Graphics Forum 35*, 3 (2016), 141–150. 5

[SLK*17] Smit N., Lawonn K., Kraima A., DeRuiter M., Sokooti H., Bruckner S., Eisemann E., Vilanova A.: Pelvis: Atlas-based surgical planning for oncological pelvic surgery. *IEEE Transactions on Visualization and Computer Graphics 23*, 1 (2017), 741–750. 6

[SPB07] Snook L., Plewes C., Beaulieu C.: Voxel based versus region of interest analysis in diffusion tensor imaging of neurodevelopment. *NeuroImage 34*, 1 (2007), 243–252. 1

[SZD*10] Sanyal J., Zhang S., Dyer J., Mercer A., Amburn P., Moorhead R.: Noodles: A tool for visualization of numerical weather model ensemble uncertainty. *IEEE Transactions on Visualization and Computer Graphics 16*, 6 (2010), 1421–1430. 2

[War13] Ware C.: *Information visualization: perception for design*, third ed. Elsevier, 2013. 5, 6

[WMK*99] Westin C. F., Maier S. E., Khidhir B., Everett P., Jolesz F. A., Kikinis R.: Image processing for diffusion tensor magnetic resonance imaging. In *MICCAI*. Springer, 1999, pp. 441–452. 2, 5

[WMK13] Whitaker R. T., Mirzargar M., Kirby R. M.: Contour boxplots: A method for characterizing uncertainty in feature sets from simulation ensembles. *IEEE Transactions on Visualization and Computer Graphics 19*, 12 (2013), 2713–2722. 2

[WWHT07] Whitcher B., Wisco J. J., Hadjikhani N., Tuch D. S.: Statistical group comparison of diffusion tensors via multivariate hypothesis testing. *Magnetic Resonance in Medicine 57*, 6 (2007), 1065–1074. 1

[ZSL*16] Zhang C., Schultz T., Lawonn K., Eisemann E., Vilanova A.: Glyph-based comparative visualization for diffusion tensor fields. *IEEE Transactions on Visualization and Computer Graphics 22*, 1 (2016), 797–806. 1, 2, 3, 4, 5, 6, 7

[ZYAG06] Zhang H., Yushkevich P. A., Alexander D. C., Gee J. C.: Deformable registration of diffusion tensor MR images with explicit orientation optimization. *Medical Image Analysis 10*, 5 (2006), 764–785. 9